NANO · MICRO small
www.small-journal.com

Controlled Synthesis of SnO_2 Nanostructures as Alloy Anode via Restricted Potential Toward Building High-Performance Dual-Ion Batteries with Graphite Cathode

Parvathy Jayan, Anil Anjali, Sangho Park, Yun-Sung Lee, and Vanchiappan Aravindan**

Dedicated to Prof. Satishchandra Ogale on the occasion of his 70th birthday

Dual-ion batteries (DIBs) are considered one of the promising energy storage devices in which graphite serves as a bi-functional electrode, i.e., anode and cathode in the aprotic organic solvents. Unlike conventional lithium-ion batteries (LIBs), DIBs reversibly store the cations and anions in the anode and cathodes during redox reactions, respectively. The electrolyte is a source for both cations and anions, so the choice of electrolyte plays a vital role. In the present work, the synthesis of SnO_2 nanostructures is reported as a possible alternative for graphite anode, and the Li-storage performance is optimized in half-cell (Li/SnO_2) assembly with varying amounts of conductive additive (acetylene black) and limited working potential (1 V vs Li). Finally, a DIB using recovered graphite (RG) fabricated from spent LIB as a cathode and SnO_2 nanostructures as an anode under balanced loading conditions. Prior to the fabrication, both electrodes are pre-cycled to eliminate irreversibility. An in-situ impedance study has been employed to validate the passivation layer formation during the charge-discharge process. The high-performance SnO_2/RG-based DIB delivered a maximum discharge capacity of 380 mAh g^{-1}. The electrochemical performance of DIB has been assessed by varying temperature conditions to evaluate their suitability in different climatic conditions.

1. Introduction

Energy deficiency is a major global concern, and the development of efficient, sustainable energy sources has become a topic of discussion. The contemporary world is experiencing the transformation from non-renewable fossil fuels to renewable energy sources such as solar, wind, hydrothermal, etc. The efficient storage of these energies is a major concern. Exploiting electrochemical energy storage devices is critical in meeting the increasing energy demands of society by reducing our reliance on fossil fuels and mitigating the impacts of climate change. Electrochemical energy storage devices, such as batteries and capacitors, have emerged as a key solution for efficient energy storage and utilization. Demand for higher energy density, faster charging times, low cost, etc., has driven the development of better electrochemical energy storage devices.[1]

Lithium-ion batteries (LIBs), which use the "rocking-chair" mechanism, have been the preferred choice for electric vehicles and consumer electronics due to their stable cycling performance, low self-discharge, and high energy density.[2–4] However, the increasing cost of raw materials (lithium, cobalt, etc.) and their environmental impact have prompted the need for a potential alternative. Dual ion batteries (DIBs) are one of the emerging energy storage devices with fast charge-discharge and efficient energy storage. In DIBs, both types of ions, i.e., cations and anions, are stored respectively in the anode and cathode during the charging process and are released back to the electrolyte medium during discharge.[5–7] The studies in the field of DIBs started with anode and cathode being graphite and a suitable electrolyte to provide ions for conduction. This subcategory of DIB is commonly called graphite-based dual-ion batteries (G-DIBs).[8,9] The graphite can undergo reversible oxidation and reduction reactions, making it suitable for both halves of a G-DIB. The equivalent DIB reactions based on graphite electrodes can be explained as follows[10]:

$$\text{Anode}: C + xLi^+ + xe^- \rightarrow Li_xC \quad (1)$$

$$\text{Cathode}: C + xA^- \rightarrow A_xC + xe^- \quad (2)$$

$$\text{Overall reaction}: xLi^+ + xA^- + C + C \leftrightarrow Li_xC + A_xC \quad (3)$$

P. Jayan, A. Anjali, V. Aravindan
Department of Chemistry
Indian Institute of Science Education and Research (IISER)
Tirupati 517507, India
E-mail: aravindan@iisertirupati.ac.in
S. Park
Department of Battery Engineering
Dongshin University
Jeollanam-do 58245, Republic of Korea
Y.-S. Lee
School of Chemical Engineering
Chonnam National University
Gwang-ju 61186, Republic of Korea
E-mail: leeys@chonnam.ac.kr
The ORCID identification number(s) for the author(s) of this article can be found under https://doi.org/10.1002/smll.202305309

DOI: 10.1002/smll.202305309

where *C* stands for carbon and *A* stands for anions. The intercalation of anions into graphite interlayers started with the discovery of graphite-intercalated compounds (GICs) in the early 1930s.[11,12,13] During the charging process, anions such as PF_6^-, BF_4^-, and $AlCl_4^-$ intercalate into the graphite layers at a higher voltage of 5.2 V vs Li.[14] On the other side, the development of graphitic anode began later in the 1980s and gained huge success. Even though graphite as an electrode material has advantages, but it exhibits some issues, such as exfoliation and volume expansion. The occurrence of exfoliation or flaking is caused by the continuous intercalation of large cations, such as Li-ions, into the graphite layers. The insertion of cations (e.g., Li) resulted in the formation of LiC_6, which would cause a volume expansion of 13%.[15] Practically, the graphite delivers a low specific capacity of ≈350 mAh g^{-1}.[16,17] Various other anode materials have been explored to replace graphite anode to attain a better capacity delivery. The metallic foils of Li, K, and Al have been used as anode materials for DIBs.[10,18]–[20] Among other types of anode materials, alloying materials have gained attention recently due to their ability to store metal cations efficiently. Switching from metallic to sulfide and oxides, quite a few research studies have been reported in the field of DIBs, especially alloying materials as the anode. A novel aluminum graphite DIB was reported in 2016 based on the alloying nature of Al, which delivered a reversible capacity of 100 mAh g^{-1}.[21] Ji et al.[22] reported a K-ion-based DIB in which Sn foil acted as an anode with a specific capacity of 66 mAh g^{-1} over a potential window of 3.0–5.0 V vs K. Layered SnS_2 has been proven to be an excellent anode against graphite in Li-based solutions exhibiting a discharge capacity of 130 mAh g^{-1}.[23]

Our work reports the SnO_2/recovered graphite from spent LIBs (RG)-based DIB using 1 M $LiPF_6$ in dimethyl carbonate (DMC) with 5% fluoroethylene carbonate (FEC) as the electrolyte. The details about the recovery were extensively described in our previous work.[24] The SnO_2 nanostructures were synthesized via a hydrothermal method and extensively characterized. In the case of DIBs, it is well established that the electrolyte plays a major role since it is the sole source of ions for conduction. The challenges faced by electrolytes are also numerous, such as the decomposition at high & low voltage conditions. Among other challenges, the inability to use a cyclic carbonate solvent such as ethylene carbonate (EC) is notable. The EC forms a cathode electrolyte interphase (CEI), which restricts the intercalation of PF_6^- into graphite interlayers, whereas the anode requires a stable solid electrolyte interphase (SEI) formation for the operation.[25] An electrolyte additive FEC (5%) is used to attain such an SEI formation, in which an inorganic layer (primarily LiF moieties) prior to other organic layers can act as an electrical insulator and facilitate Li-ions conduction.[26–29] The SnO_2 nanostructures store these Li^+ ions via an alloying mechanism, and PF_6^- anions intercalate into interlayer spaces of RG, which has expanded interlayer spacing due to previous ion insertions.[30–33] In half-cell assembly with optimized loading of the conductive additive (40%), the SnO_2 displayed a maximum reversible capacity of ≈846 mAh g^{-1} in the absence of EC. After the electrochemical pre-treatment, the DIB is assembled with RG cathode and SnO_2 anode under balanced mass loading conditions. Finally, the full cell delivered an energy density of ≈143 Wh kg^{-1} at ambient temperature conditions. The electrochemical activity of DIB at various temperature conditions is studied and discussed in detail.

2. Results and Discussion

Figure 1a-b shows the surface morphological characteristics of the hydrothermally synthesized SnO_2 nanostructures. SnO_2 nanostructures in the form of rods are visible in the FE-SEM images, and both ends of the rods were severed and seemed to be fragments of a larger one (Figure 1b). The presence of rod-shaped morphologies is evident from the TEM pictures as well (Figure 1c-d). The high-resolution TEM pictures highlight the SnO_2 in its clearly defined crystalline phase. These HR-TEM pictures (Figure 1e) were used to compute the *d*-spacing of lattice fringes, which was determined to be 0.357 nm. The appearance of the diffusive rings in the chosen area electron diffraction pattern (SAED) is consistent with the polycrystalline structure of SnO_2 (Figure 1f). As a result, diffusive rings are observed rather than bright spots. The EDS mapping also observed the homogeneous distribution of the Sn and O elements (Figure 1g-h). SEM images of both SnO_2 and RG active materials were recorded after the galvanostatic charge-discharge studies (Figure S1, Supporting Information). It is evident from the figure that both SnO_2 and RG got bound well with conductive carbon and binder. Also, a less significant change in the morphology of SnO_2 is noted.

The sharp reflections (110), (101), and (211) observed at corresponding 2θ values 26.58, 33.89, and 51.78 from XRD (**Figure 2a**) show good crystallinity of the SnO_2 nanostructures with tetragonal structure. With lattice parameter values were calculated and found to be $a = b = 4.7375$ and $c = 3.188$ Å. Apparently, no secondary peaks corresponding to the impurities or different phases of SnO_2 were observed. This demonstrates categorically that the hydrothermal procedure is one of the effective methods for producing phase-pure SnO_2 nanostructures. Using Scherrer's equation ($D = 0.9\lambda/\beta \cos\theta$), the crystallite size was determined to be 14.9 nm. From surface area analysis, the specific surface area and pore radius of SnO_2 nanostructures are estimated to be ≈22.2 m^2 g^{-1} (Figure 2b) and ≈56.9 Å, respectively. The oxidation state of the chemical species is investigated using X-ray photoelectron spectroscopy (XPS), particularly on the surface of the SnO_2 nanostructures (Figure 2c-e). Peaks observed at 486.8 and 495.1 eV, which correspond to Sn $3d_{5/2}$ and Sn $3d_{3/2}$ (Figure 2c), respectively, can be seen in the deconvoluted Sn 3d spectra, indicating that Sn is in the 4+ oxidation state.[36,37] The binding energy of the 3rd electron of Sn is related to the difference in energy between the Sn $3d_{5/2}$ and Sn $3d_{3/2}$ states (8 eV). The three asymmetric peaks in the O 1s spectrum correspond to the environments Sn–O, C–O, and O–C=O, respectively, appearing at 530.5, 531.4, and 532.5 eV (Figure 2d). Similar to this, the measured binding energies for the C 1s spectra of 284.8, 286.4, and 288.9 eV, respectively, correspond to carbonyl carbon (C=O) and sp^3 carbon.

The galvanostatic charge-discharge curves of various Li/SnO_2 composites were studied in the half-cell assembly at a current density of 60 mA g^{-1} within a potential window of 0.005–1 V vs Li (**Figure 3a**) and (Figure S2, Supporting Information). Amongst, the Li/SnO_2@40C delivered a maximum reversible capacity of ≈846 mAh g^{-1}. The carbon present in the composite mitigated the poor conductivity issue of amorphous Li_2O formed during the decomposition of SnO_2. The carbon support also serves as an elastic layer that buffers the volume change during the charge-discharge process, thus inhibiting the so-called pulverization of

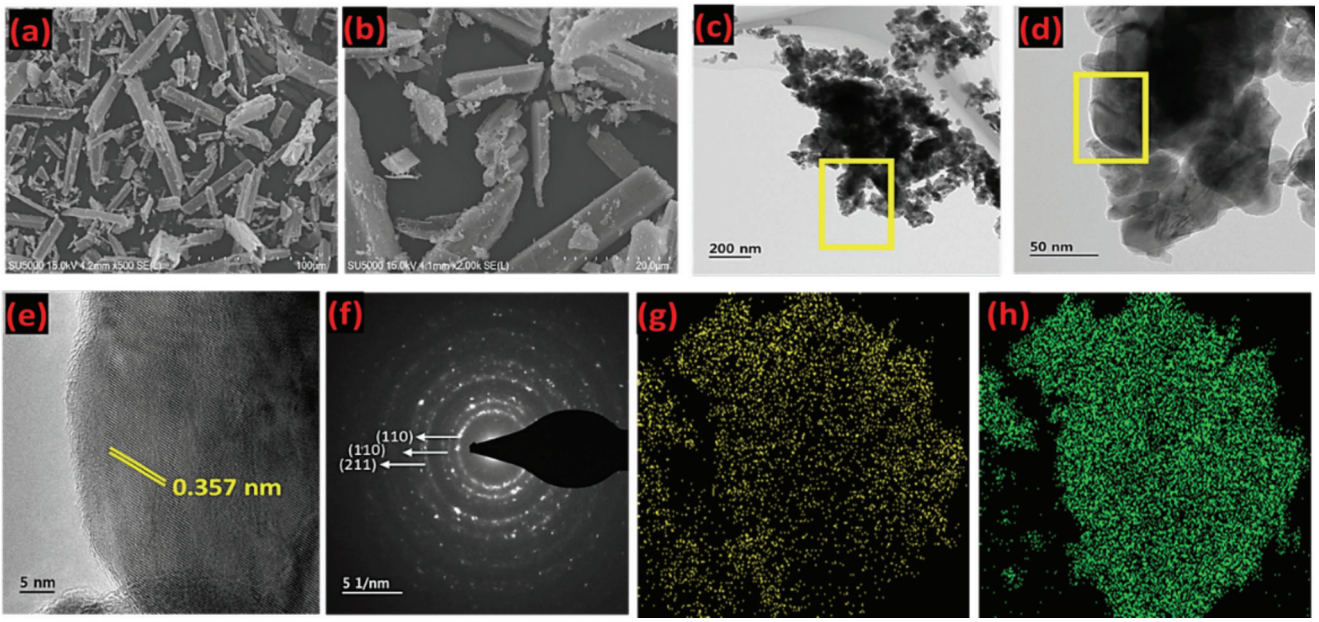

Figure 1. a,b) FE-SEM image of SnO_2 nanostructures prepared by hydrothermal approach, c,d) TEM images, e) HR-TEM image of SnO_2 nanostructures with lattice fringes, f) SAED pattern of SnO_2 nanostructures, and g,h) Elemental mapping of SnO_2 nanostructures.

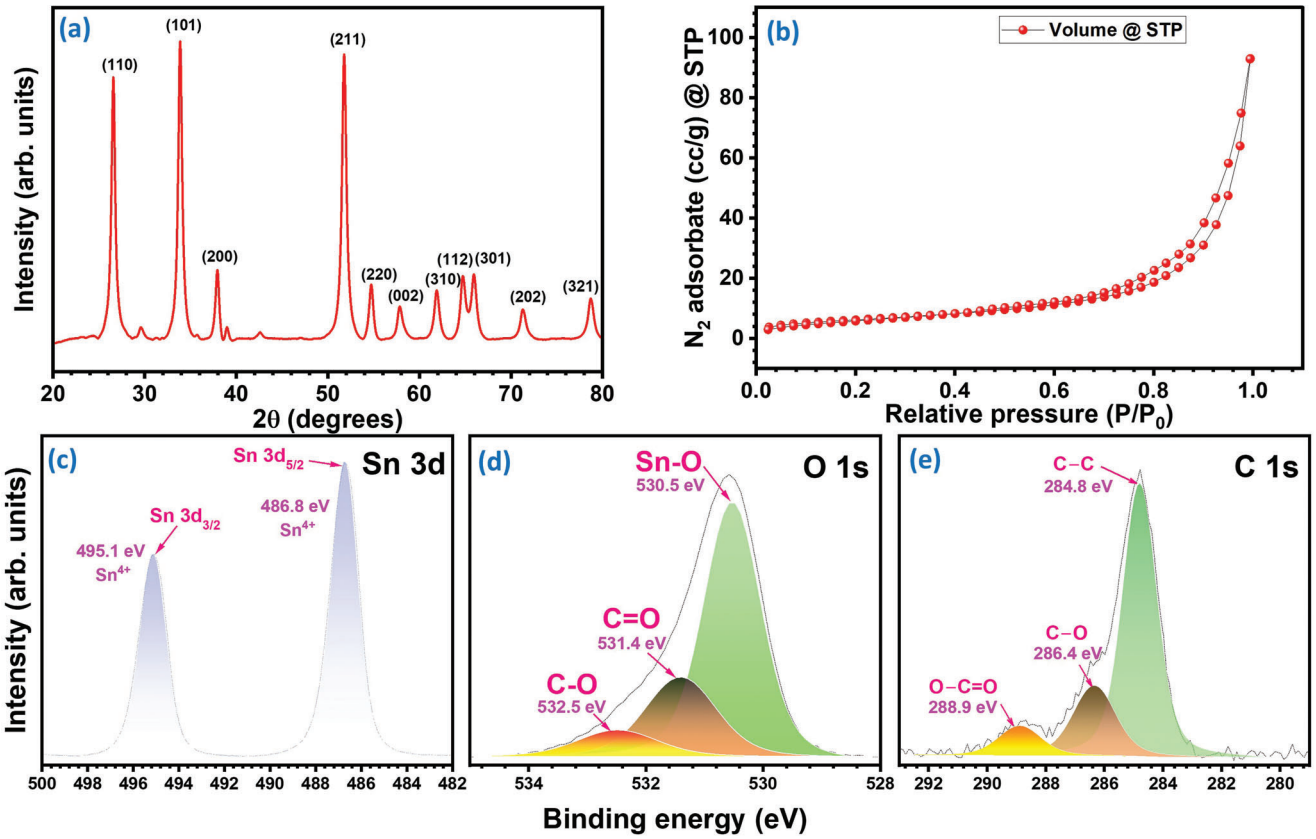

Figure 2. a) XRD of SnO_2 nanostructures, b) N_2-adsorption/desorption isotherms; deconvoluted XPS spectra of SnO_2 c) Sn 3d, d) O 1s, and e) C 1s.

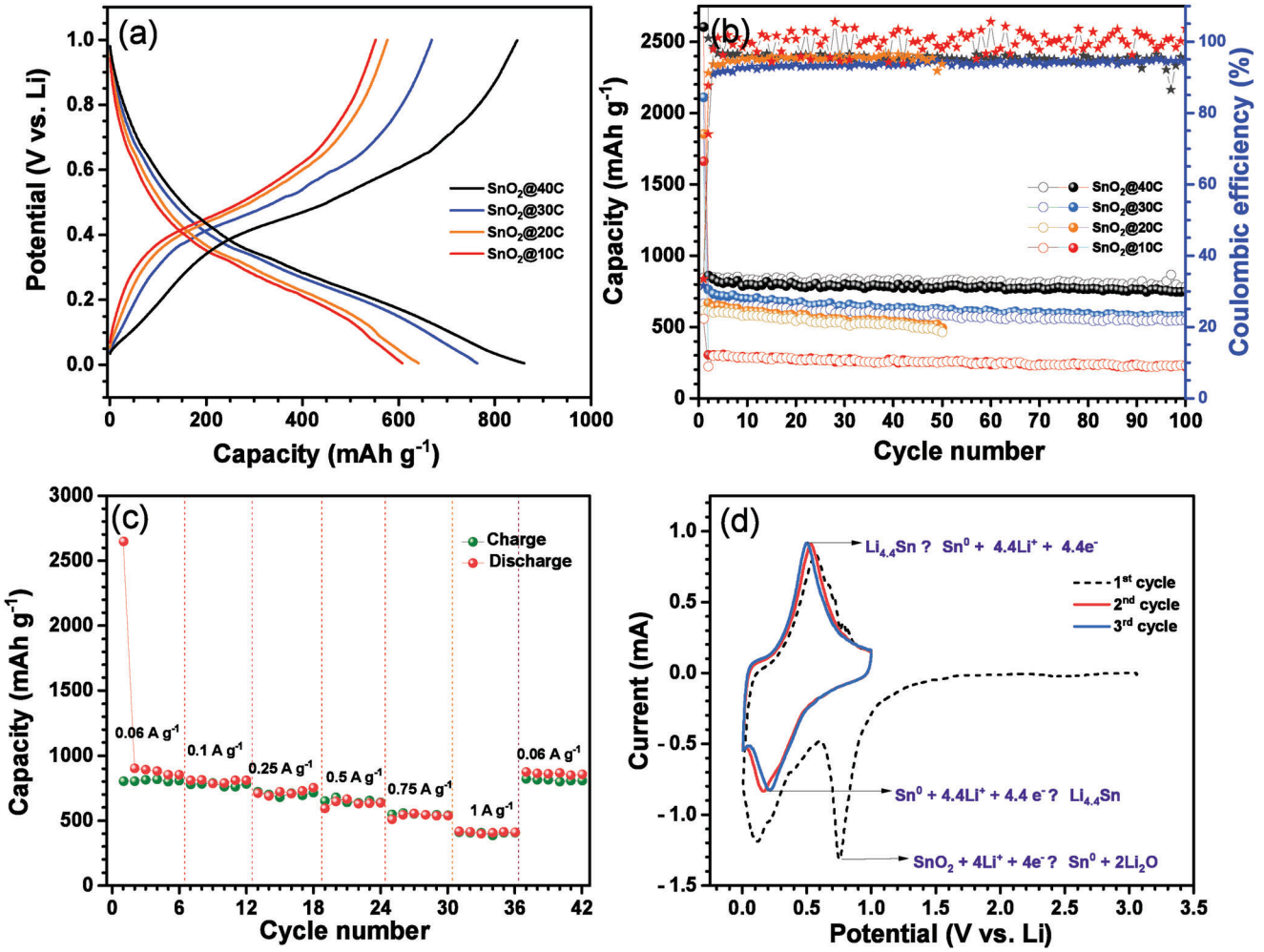

Figure 3. a) Voltage vs Capacity profile of SnO_2 nanostructures with different carbon ratios, b) capacity vs Cycle number profile of SnO_2 nanostructures with different carbon ratios, c) rate performance of SnO_2@40C at the different current rate, and d) typical CV traces of SnO_2@40C nanostructures at the scan rate of 0.1 mV s^{-1}.

the electrode material. It is evident from capacity vs cycle number plots (Figure 3b) that increased carbon content provided cyclic stability to the performance of SnO_2 anode material. After 50 cycles, the composite retained cyclic stability with capacity stability of up to 95% when compared with other composites and bare SnO_2 (Figure S3, Supporting Information). In cyclic voltammetry (CV) of SnO_2@40C, the prominent reduction peak at ≈0.7 V vs Li is indeed due to the decomposition of both SnO_2 and electrolyte solution. This decrease peak is frequently referred to as the "formation peak" or the "SEI-forming peak" because it relates to the creation of the SEI layer on the electrode's surface. Despite the irreversible consumption of Li-ions, forming the SEI layer is an important step in the overall electrochemical reaction as it acts as a passivation layer, preventing further electrolyte decomposition and protecting the electrode from further degradation. The cathodic peak observed at ≈0.2 V vs Li corresponds to the formation of the alloy with Li ($Sn^0 + Li \leftrightarrow Li_xSn$) (Figure 3d).[38,39] The anodic peak observed at 0.5 V vs Li corresponds to the de-alloying reaction ($Li_xSn \leftrightarrow Sn^0 + Li$) from the Li_xSn alloy, and eventually, the metallic Sn (Sn^0) is reconstituted. The potential range of 1 V vs Li prevents the metallic Sn from further oxidizing into its oxide derivatives (SnO and SnO_2), i.e., limiting the alloying/de-alloying process.[38] The notable and merged peaks in the CV traces indicate the durability of the SnO_2@40C composite.

The in-situ electrochemical impedance investigation of Li/SnO_2@40C, which collected data over the 1st, 2nd, 5th, 10th, and 25th cycles, revealed the SEI development and its stability over the cycles (**Figure. 4**). We observed a greater charge transfer resistance (R_{CT}) after the first cycle, primarily because of the formation of the SEI layer, which caused an irreversible capacity loss in the first cycle (Figure S5 and Table S1, Supporting Information). The R_{CT} values appear to be higher irrespective of the charge or discharge process at the lower cut-off potential of 5 mV vs Li due to the SEI layer expansion and limited electrical conductivity of the Li_xSn alloy compared to its metallic state (Sn^0). When the cell potential reaches the upper cut-off potential of 1 V vs Li, a considerable reduction in the R_{CT} is observed, which originates in the depletion of the SEI layer. Also, the presence of metallic Sn^0 aids in reducing the R_{CT} values and is worth mentioning. The formation and depletion of the SEI layer

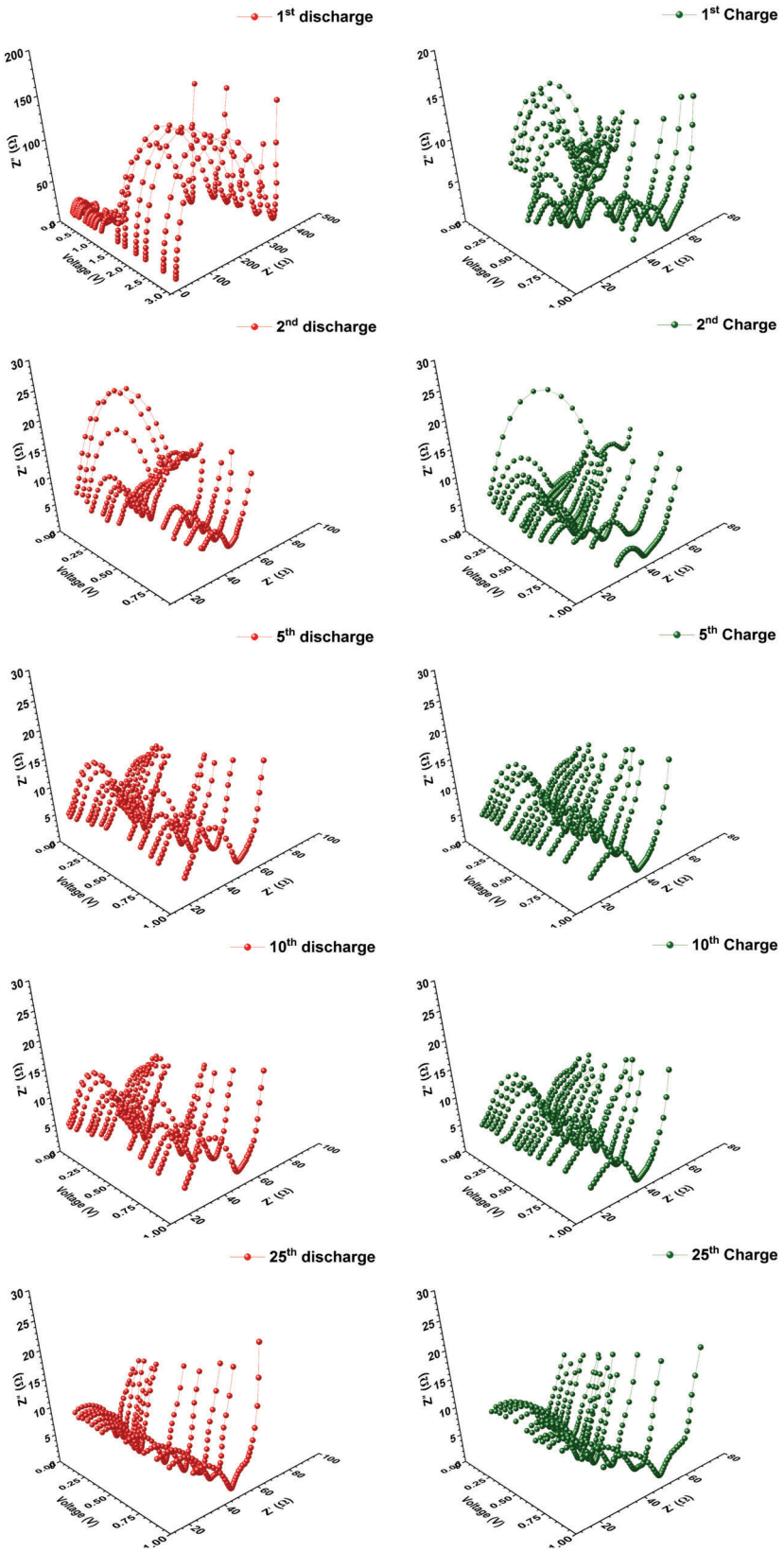

Figure 4. An *in-situ*-EIS profile of Li/SnO_2@40C half-cell. EIS traces of 1st, 2nd, 5th, 10th, and 25th charge-discharge cycles at various potential intervals.

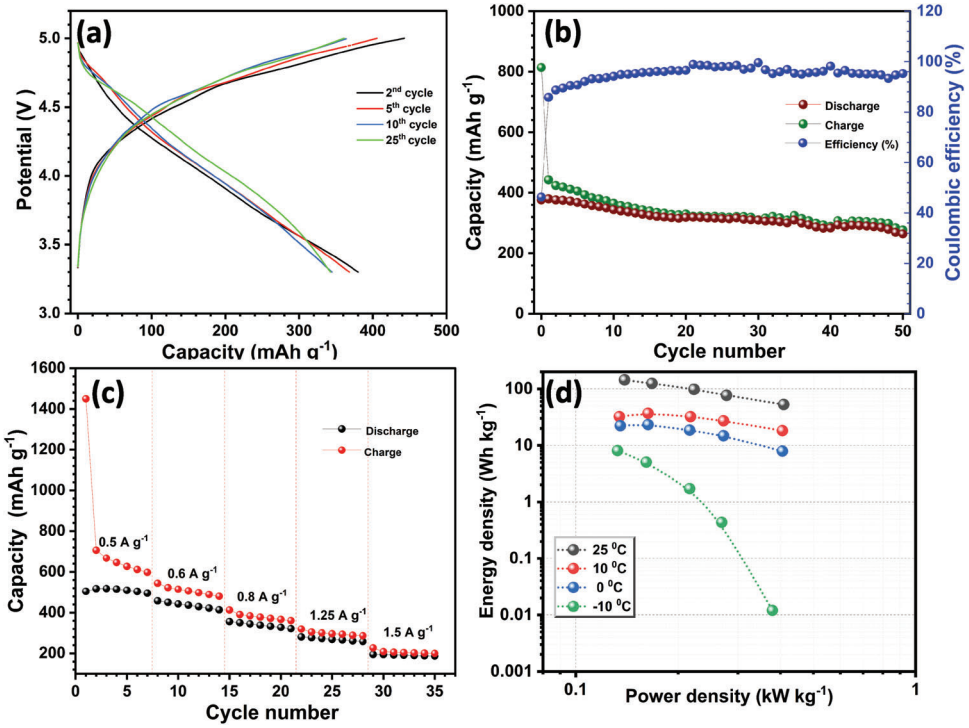

Figure 5. a) Voltage vs Capacity profile of SnO_2/RG DIB, b) capacity vs rycle profile of SnO_2/RG cell, c) Rate performance of SnO_2/RG cell, and d) energy density and power density represented by Ragone plot at various temperatures SnO_2/RG-based DIB.

are validated with more or less constant R_{CT} values trend during the charge-discharge process. After the initial charge-discharge, a lower and more stable R_{CT} value was discovered at 1 V vs Li, and it persisted up until the measured 25th cycle. The consistency of R_{CT} values reciprocates the formation of a stable and durable SEI layer over the electrode surface.[35] The attaining stable and robust SEI layer over the SnO_2 electrode in the absence of EC is a significant improvement possible with a slightly higher conductive additive, limited working potential, and electrolyte additive, FEC.

In this line, we attempted to build the complete DIB using the synthesized SnO_2 nanostructures as an anode and graphite as a cathode. Prior to the formation of full-cell, the anode and cathode underwent three cycles of pretreatment with metallic Li to eliminate the irreversibility. The mass loading for the anode-to-cathode ratio was fixed at 0.9:11, and the CR2016 coin cell was assembled using fresh electrolyte 1 M $LiPF_6$ in DMC with 5% FEC. A substantial mass loading is required for the cathode side due to the significantly higher specific capacity of anode material significantly higher specific capacity than that of cathode materials (Figure S4, Supporting Information). At a current density of 1 A g^{-1}, typical galvanostatic studies were performed for the full-cell SnO_2/RG. With respect to anode loading for a second discharge, in the potential window of 3.3 to 5 V, the SnO_2/RG cell delivered a capacity of 380 mAh g^{-1} (**Figure 5a**), which is calculated based on the least mass loading, i.e., SnO_2. Due to the creation of an unstable SEI layer in the first cycle and the usage of fresh electrolyte, which requires a few cycles for stabilization. Nevertheless, the full-cell experiences an irreversible capacity loss after the electrochemical pretreatment. The CV traces clearly indicate the redox reaction of the DIB (Figure S6, Supporting Information). After the first cycle, coulombic efficiency in SnO_2/RG DIB is maintained at >90% for 50 cycles (Figure 5b). The DIBs rendered capacity retention of ≈62% with capacity fading at the end of the 50th cycle, which is evident due to the was evident predominantly because of the electrolyte decomposing at a high voltage of 5 V. Rate performance studies were performed for the SnO_2/RG cell, in which the coloumbic efficiency increases with the high current rate. This clearly implies that the DIBs are perfectly suited for high-power applications. The galvanostatic charge-discharge studies were also evaluated at different temperatures for the full cell at a current density of 1 A g^{-1}, and it was found that the full-cell shows better capacity at room temperature, 25 °C (Figure S7, Supporting Information). The EIS spectrum for the full-cell is also recorded before and after cycling, and it is observed that the R_{CT} value increases after cycling (Figure S8, Supporting Information). The energy and power densities of DIB under various conditions of current density and temperature were evaluated using a Ragone plot (Figure 5d), for which the combined mass of the active components in the anode and cathode is taken into account. At room temperature (25 °C), the SnO_2/RG DIB performs better, producing a maximum energy density of roughly 143 Wh kg^{-1}. However, the energy density drops due to electrolyte freezing and ion movement restriction at lower temperatures (−10, 0, and 10 °C), reaching 8.09 Wh kg^{-1} at the lowest temperature (−10 °C). The potential for employing SnO_2 nanostructures as a potential anode in DIB applications was well demonstrated by this exploratory investigation. The expanded interlayer spacing present in RG also favored the intercalation of PF_6^- into it during charging.[40,41]

3. Conclusion

In this work, we were able to convincingly show that SnO_2 nanostructures might be used as an anode in dual ion battery applications. Using a simple hydrothermal procedure, we successfully synthesized SnO_2 nanostructures, delivering a maximum reversible capacity of 860 mAh g^{-1}. From the half-cell studies of synthesized SnO_2 nanostructures, it is in agreement that by increasing the ratio of conductive carbon in the electrode, better performance of the active material can be attained. Li_2O generated during the irreversible stage of SnO_2 conversion to metallic Sn was less influential due to the presence of carbon. Subsequently, using the SnO_2 nanostructures, a standard dual ion cell, SnO_2/RG, is capable of generating a specific capacity of 380 mAh g^{-1} based on anode mass loading. The full-cell rendered the maximum energy density of ≈143 Wh kg^{-1} at ambient temperature conditions with a decent cycling profile. The larger interlayer gap made the intercalation of PF_6^- into RG during charging more convenient. The performance of both DIBs is noteworthy overall, and additional research is being done to improve the performance of DIBs in terms of cycle stability and electrolyte stability. The performance of both DIBs is noteworthy overall, and additional research is required to improve the performance of DIBs in terms of cycle stability and electrolyte stability.

4. Experimental Section

Synthesis of SnO_2 Nanostructures: The synthesis of SnO_2 nanostructures was carried out using a conventional hydrothermal process. The primary reagents employed were $SnCl_2$ (Sigma-Aldrich) and $C_2H_2O_4 \cdot 2H_2O$ (Sigma-Aldrich). The reagents were separately dissolved in distilled water for 30 min using a magnetic bead and a stirrer. The two solutions were then combined and swirled for a further 15 min. The solution mixture is poured into a 50 ml Teflon-lined stainless-steel autoclave and heated at 140 °C for 12 h in a box furnace. After cooling, the product obtained was subjected to centrifugation and rinsed repeatedly using water and ethanol. The supernatant is discarded, and the pellet is kept at 80 °C for drying and further heated at 400 °C for 10 h to obtain SnO_2 powder. The undergoing mechanism in the formation of SnO_2 is as follows.[34]

$$Sn^{2+} + C_2O_4^{2-} \rightarrow SnC_2O_4 \quad (4)$$

$$SnC_2O_4 + O_2 \rightarrow SnO_2 + CO_2 \quad (5)$$

Material Characterization: Using Rigaku D/teX Ultra 250 diffractometers (40 kV, 200 mA, $\lambda = 1.5406$) and Powder X-ray diffraction (XRD) with Cu Kα radiation, the structural investigation was carried out. The field-emission scanning electron microscope (FE-SEM S-4700, Hitachi, Japan) was used to examine the surface morphology of the SnO_2 nanostructures. The high-resolution transmission electron microscope (HR-TEM, TECNAI, Philips, the Netherlands, 200 keV) was used to assess the interior structure. To determine the elements present, X-ray photoelectron spectroscopy (XPS; Multilab 2000, UK; monochromatic Al K radiation hv = 1486.6 eV) was used. Energy-dispersive X-ray spectroscopy (EDS) was also employed in addition to the observed data. To understand the surface area of particles Quantachrome – BET Surface area analyzer was used.

Electrode Fabrication and Cell Assembly: Handmade electrodes were made with various proportions of active material (SnO_2 nanostructures), conductive carbon (acetylene black), and binder (Teflonized acetylene black) using a mortar and pestle. 8 mg SnO_2 (active material), 1 mg acetylene black (conductive carbon), and 1 mg teflonized acetylene black (TAB-2, binder) were mixed using ethanol to form a free-standing film. This thin film was then pressed onto a stainless steel mesh (Goodfellow, UK), having a diameter of 14 mm and a nominal aperture of 0.38 mm. The stainless steel mesh plays the role of a current collector for the electrode. The percentage of conductive carbon was increased by 10% (denoted by SnO_2@10C (8:1:1), SnO_2@20C (7:2:1), SnO_2@30C (6:3:1), and SnO_2@40C (4:4:2)) during the formulation of the electrode. However, the binder ratio was fixed at 10%. Half cells were fabricated against metallic Li as Li/SnO_2 and Li/RG. Mass loading on both electrodes was properly balanced prior to full-cell fabrication, and both electrodes received three separate cycles of pre-treatment with metallic Li. After three cycles, the cells were dismantled, and the SnO_2 electrode was paired against the RG electrode to build SnO_2/RG DIB. All the electrodes were dried in a heated vacuum oven for four hours before the cell fabrication. The cell fabrication processes were conducted in an argon-filled glove box (MBraun, Germany, $O_2 < 0.1$ ppm and $H_2O < 0.1$ ppm), and the cells were fabricated using CR 2016-coin cells in 1 M $LiPF_6$ in DMC (Sigma Aldrich) and 5% FEC (Sigma-Aldrich). For Li/SnO_2 and Li/RG (Figure S2, Supporting Information), the half-cells were evaluated in the potential windows of 0.005–1 V vs Li and 3–5.2 V vs Li. Galvanostatic charge-discharge and in-situ electrochemical impedance studies were recorded using a Biologic BCS 805 (France) battery tester. Additionally, the environmental chamber (Espec, Japan) was used to assess the temperature-dependent performance of DIB.

Supporting Information

Supporting Information is available from the Wiley Online Library or from the author.

Acknowledgements

Y.S.L. acknowledges the financial support from the National Research Foundation of Korea (NRF) grant funded by the Korean government (Ministry of Science, ICT & Future Planning) (No. RS-2023-00208361). V.A. acknowledges financial support from the Science and Engineering Research Board, a statutory body of the Department of Science and Technology (DST), Govt. of India, through Swarnajayanti Fellowship (SB/SJF/2020-21/12) and Nanomission (DST/NM/TUE/EE-03/2019-1G-IISERTp).

Conflict of Interest

The authors declare no conflict of interest.

Data Availability Statement

The data that support the findings of this study are available from the corresponding author upon reasonable request.

Keywords

alloying, anodes, dual-ion batteries, graphite cathodes, recycling spent lithium-ion batteries (LIBs), SnO_2

Received: June 26, 2023
Revised: September 15, 2023
Published online:

[1] G. Jeong, Y.-U. Kim, H. Kim, Y.-J. Kim, H.-J. Sohn, *Energy Environ. Sci.* **2011**, *4*, 1986.

[2] Y. Chen, Y. Kang, Y. Zhao, L. Wang, J. Liu, Y. Li, Z. Liang, X. He, X. Li, N. Tavajohi, B. Li, *J. Energy Chem.* **2021**, *59*, 83.
[3] T. Placke, R. Kloepsch, S. Dühnen, M. Winter, *J. Solid State Electrochem.* **2017**, *21*, 1939.
[4] T. Kim, W. Song, D.-Y. Son, L. K. Ono, Y. Qi, *J. Mater. Chem. A Mater.* **2019**, *7*, 2942.
[5] T. Placke, A. Heckmann, R. Schmuch, P. Meister, K. Beltrop, M. Winter, *Joule* **2018**, *2*, 2528.
[6] *Beyond Conventional Batteries: Strategies towards Low-Cost Dual-Ion Batteries with High Performance* https://doi.org/10.1002/anie.201814294.
[7] K. V. Kravchyk, M. V. Kovalenko, *Adv. Energy Mater.* **2019**, *9*, 1901749.
[8] R. Santhanam, M. Noel, *J. Power Sources* **1998**, *76*, 147.
[9] R. Santhanam, M. Noel, *J. Power Sources* **1995**, *56*, 101.
[10] L. Zhang, H. Wang, X. Zhang, Y. Tang, *Adv. Funct. Mater.* **2021**, *31*, 2010958.
[11] U. Hofmann, Graphit Und Graphitverbindungen, in *Ergebnisse der Exakten Naturwissenschaften*, Springer Berlin Heidelberg, Berlin, Heidelberg, **2007**, pp. 229-256.
[12] M. Noel, R. Santhanam, *J. Power Sources* **1998**, *72*, 53.
[13] http://refhub.elsevier.com/S2542-4351(18)30406-9/sref84, **2023**.
[14] R. T. Carlin, H. C. De Long, J. Fuller, P. C. Trulove, *J. Electrochem. Soc.* **1994**, *141*, L73.
[15] S. Schweidler, L. De Biasi, A. Schiele, P. Hartmann, T. Brezesinski, J. Janek, *J. Phys. Chem. C Nanomater Interfaces* **2018**, *122*, 8829.
[16] C. Wang, H. Zhao, J. Wang, J. Wang, P. Lv, *Ionics* **2013**, *19*, 221.
[17] J. Asenbauer, T. Eisenmann, M. Kuenzel, A. Kazzazi, Z. Chen, D. Bresser, *Sustainable Energy Fuels* **2020**, *4*, 5387.
[18] L.-N. a Wu, J. Peng, Y.-K. Sun, F.-M. Han, Y.-F. Wen, C.-G. Shi, J.-J. Fan, L. Huang, J.-T. Li, S.-G. Sun, *ACS Appl. Mater. Interfaces* **2019**, *11*, 18504.
[19] K. V. Kravchyk, P. Bhauriyal, L. Piveteau, C. P. Guntlin, B. Pathak, M. V. Kovalenko, *Nat. Commun.* **2018**, *9*, 4469.
[20] K. V. Kravchyk, M. V. Kovalenko, *Adv. Energy Mater.* **2020**, *10*, 2002151.
[21] X. Zhang, Y. Tang, F. Zhang, C.-S. Lee, *Adv. Energy Mater.* **2016**, *6*, 1502588.
[22] B. Ji, F. Zhang, X. Song, Y. Tang, *Adv. Mater.* **2017**, *29*, 1700519.
[23] Y.-B. Fang, W. Zheng, T. Hu, L. Li, W.-H. Yuan, *ACS Omega* **2022**, *7*, 7616.
[24] M. L. Divya, S. Natarajan, Y. S. Lee, V. Aravindan, *ChemSusChem* **2020**, *13*.
[25] H. Wang, M. Yoshio, *Chem. Commun.* **2010**, *46*, 1544.
[26] S. S. Zhang, *J. Power Sources* **2006**, *162*, 1379.
[27] T. Hou, G. Yang, N. N. Rajput, J. Self, S.-W. Park, J. Nanda, K. A. Persson, *Nano Energy* **2019**, *64*, 103881.
[28] J. A. Read, A. V. Cresce, M. H. Ervin, K. Xu, *Energy Environ. Sci.* **2014**, *7*, 617.
[29] E. Markevich, G. Salitra, D. Aurbach, *ACS Energy Lett.* **2017**, *2*, 1337.
[30] X. Ma, M. Chen, B. Chen, Z. Meng, Y. Wang, *ACS Sustainable Chem. Eng.* **2019**, *7*, 19732.
[31] J. Yang, E. Fan, J. Lin, F. Arshad, X. Zhang, H. Wang, F. Wu, R. Chen, L. Li, *ACS Appl. Energy Mater.* **2021**, *4*, 6261.
[32] M. L. Divya, S. Natarajan, Y.-S. Lee, V. Aravindan, *ChemSusChem* **2020**, *13*, 5654.
[33] S. Natarajan, M. L. Divya, V. Aravindan, *J Energy Chem* **2022**, *71*, 351.
[34] Z. Wen, F. Zheng, K. Liu, *Mater. Lett.* **2012**, *68*, 469.
[35] M. Akshay, S. Praneetha, Y.-S. Lee, V. Aravindan, *Electrochim. Acta* **2023**, *439*, 141599.
[36] X. Rong, D. Chen, G. Qu, T. Li, R. Zhang, J. Sun, *Sensor Actuator, B Chem* **2018**, *269*, 223.
[37] M. A. Stranick, A. Moskwa, *Surf. Sci. Spectra* **1993**, *2*, 45.
[38] V. Aravindan, K. B. Jinesh, R. R. Prabhakar, V. S. Kale, S. Madhavi, *Nano Energy* **2013**, *2*, 720.
[39] V. Aravindan, J. Sundaramurthy, E. N. Kumar, P. S. Kumar, W. C. Ling, R. Von Hagen, S. Mathur, S. Ramakrishna, S. Madhavi, *Electrochim. Acta* **2014**, *121*, 109.
[40] M. L. Divya, S. Praneetha, Y.-S. Lee, V. Aravindan, *Composites Part, B* **2022**, *230*, 109487.
[41] M. L. Divya, S. Natarajan, Y.-S. Lee, V. Aravindan, *J. Mater. Chem. A* **2020**, *8*, 4950.

